Journal of Physics:
Conference Series

Internal boundary layer development due to impulsive changes in spanwise wall velocity

Journal of Physics: Conference Series **3173** (2026) 012002 doi:10.1088/1742-6596/3173/1/012002

Internal boundary layer development due to impulsive changes in spanwise wall velocity

Max W. Knoop[1], **Rahul Deshpande**[2] **and Bas W. van Oudheusden**[1]

[1]Faculty of Aerospace Engineering, Delft University of Technology, 2629 HS Delft, The Netherlands
[2]Department of Mechanical Engineering, The University of Melbourne, Parkville, VIC 3010, Australia

E-mail: m.w.knoop@tudelft.nl

Abstract. The spatial response of a turbulent boundary layer subjected to a streamwise-periodic square-wave (SqW) variation of the spanwise wall velocity is investigated experimentally. The SqW forcing is implemented via a setup comprising 48 spanwise-running belts, which is used to assess the influence of the (viscous-scaled) forcing wavelength for: sub-optimal $\lambda_x^+ = 471$, near-optimum $\lambda_x^+ = 942$, and post-optimal $\lambda_x^+ = 1884$ conditions, at a fixed spanwise-velocity amplitude $A^+ = 12$. Previous studies have identified a high phase-wise rate-of-change of the Stokes strain (wall-normal gradient of spanwise velocity) – the Stokes-strain rate (SSR) – to drive the attenuation of turbulence, whereas recovery of turbulence was found when SSR ~ 0 extended over a sufficient fetch of the phase, referred to as subphases I and II, respectively. For the SqW, subphase-I occurs over a fixed short fetch where the sign of wall velocity reverses, whereas subphase-II extends over the rest of the half-phase, where the wall velocity remains constant. These SSR-related hypotheses are confirmed; the phase-wise variation of turbulence attenuation and recovery, however, is established only for the post-optimal case, owing to its extended fetch of subphase-II. An out-of-phase trend between C_f and the turbulence is elucidated by evaluating the internal boundary layer (IBL) thickness δ_i, where C_f and δ_i show a clear correlation. For the post-optimal regime, the IBL develops from $\delta_i^+ = 10$ to 25 over subphase-II, indicative of a thickening of the viscous sublayer, but quickly recovers to its initial value during the step-change in spanwise wall velocity in subphase-I.

1 Introduction

Spanwise wall forcing for skin-friction drag reduction (DR) in wall-bounded turbulence has been extensively investigated over the past three decades (Ricco et al., 2021). In its general formulation, this strategy imposes a streamwise-travelling wave (STW) of spanwise wall velocity: $W_w(x,t) = A\sin(k_x x - \omega t)$, with wavenumber-frequency pair $\{k_x,\ \omega\}$ and forcing amplitude A. The coordinates $\{x,\ y,\ z\}$ and the instaneneous velocities $\{U,\ V,\ W\}$ denote the streamwise, spanwise and wall-normal directions, t is time. On a narrow *high-DR ridge* in the $k_x - \omega$ plane, savings of up to 48% at $A^+ = 12$ ('+' superscript denotes viscous scaling) are reported by Quadrio et al. (2009), but a region of *drag increase also* exists when the wave speed coincides with the convection velocity of the near-wall turbulence. From the STW, two specific types of wall forcing are identified: temporal wall oscillations when $k_x = 0$ (Quadrio and Ricco, 2004; Jung et al., 1992), and steady spatial forcing when $\omega = 0$ (Viotti et al., 2009).

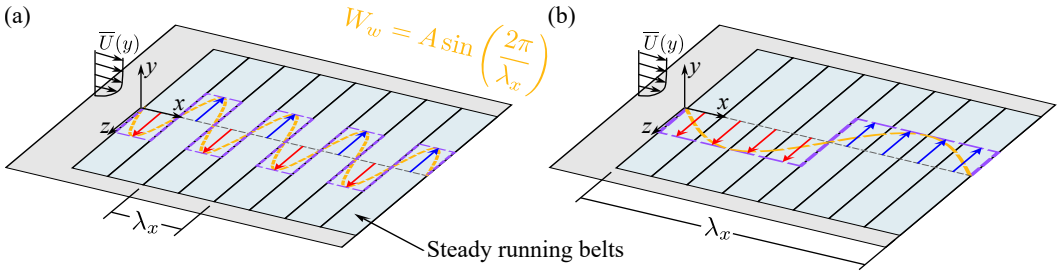

Figure 1: Schematic of the spatial wall forcing imposed via a steady sinusoidal wave (SinW; in orange) typically considered in the literature against the steady square-wave (SqW; in purple), implemented in the present experiment through discretised wall elements (in light blue). (a) and (b) illustrate the independent variation of wavelength λ_x and forcing strength A. Red (blue) arrows denote a positive (negative) spanwise wall velocity (*i.e.*, belt speed). Reproduced from Knoop et al. (2025).

For the spatial forcing, the spanwise wall velocity is imposed according to:

$$W_w(x,t) = A\sin\left(k_x x\right) = A\sin\left(\frac{2\pi}{\lambda_x}x\right), \tag{1}$$

where λ_x is the streamwise wavelength of actuation. $\lambda_x^+ \approx 1000$ corresponds to the DR optimum (Viotti et al., 2009), and is closely linked to the $T^+ = 2\pi/\omega^+ \approx 100$ optimum for temporal oscillations through a convective transformation, $\lambda_x \sim U_c^+ T^+$, with the near-wall convection velocity $U_c^+ \approx 10$ (Kim and Hussain, 1993). The spatial forcing outperforms the temporal forcing, in terms of DR, by about 20-30%, and achieves DR values that are close to the STWs (Quadrio et al., 2009; Viotti et al., 2009). So far, however, spatial forcing has received only limited attention in a small number of direct numerical simulation (DNS) studies (Ricco et al., 2021), which motivates our experimental investigation.

We experimentally investigate the response of a zero-pressure-gradient (ZPG) turbulent boundary layer (TBL) subject to a streamwise-periodic square-wave (SqW) type forcing, analogous to its sinusoidal wave (SinW) counterpart (1), which is illustrated in Figure 1. Following the concept previously introduced by the present authors (Knoop et al., 2024), the SqW boundary condition is imposed using an array of steady spanwise-running belts, rotating in an alternate sense along the streamwise direction. Unique to this experiment is the investigation across a wide range of the DR regime, at a fixed forcing amplitude $A^+ = 12$, by varying the wavelength from sub-optimal $\lambda_x^+ = 471$, to near-optimal $\lambda_x^+ = 942$, and post-optimal $\lambda_x^+ = 1884$ conditions. This feature of the wall-forcing apparatus is illustrated in Figure 1: A is directly controlled by setting the (stepless) belt velocity, while λ_x is varied by selecting the number of belts that constitute a single waveform, which is varied from 2 to 8 between tiles (a) and (b).

Knoop et al. (2025) emphasised the importance of the Stokes-strain rate (SSR) in the DR mechanism, with a primary focus on how the SSR characteristics of the SqW are related to streamwise variation of turbulence (*i.e.*, Reynolds stresses). The relevant theoretical background is reviewed in §1.1. While the focus was on the mechanism of turbulence modification, the spatial variation of the skin-friction coefficient (C_f) was also reported, which showed an out-of-phase trend with the periodic variation of the Reynolds stresses in the post-optimal regime ($\lambda_x^+ = 1884$). These results are revisited in §3. The previously reported C_f trends are elucidated in this paper. In §4, we show how local impulses of SSR by the SqW drive the growth of an internal boundary layer (IBL), which correlates well with the trend in C_f. The experimental details are provided in §2, and the concluding remarks are presented in §5.

1.1 Turbulence modification via the Stokes-strain rate

The underlying mechanism of DR remains an open point of debate. Common across numerous propositions, however, is the importance of the near-wall ($y^+ \lesssim 15$) spanwise shear layer that forms when imposing $W_w(x,t)$. The transverse shear layer is analogous to Stokes' second problem, and is well described by the laminar generalised Stokes layer (GSL) solution (Quadrio and Ricco, 2011). Eforts to uncover the DR mechanism include, for example, the interaction of the GSL with the structures associated with the self-sustaining cycle (see, *e.g.*, Baron and Quadrio, 1996; Ricco, 2004; Kempaiah et al., 2020), or the mean-vorticity dynamics induced by the GSL (Choi and Clayton, 2001).

The mechanism proposed by Leschinger and co-workers, based on the Stokes-strain rate (SSR), takes a central place in this study. The SSR is the phase-wise ($\xi \equiv x - \omega/k_x t$) rate-of-change of the Stokes strain

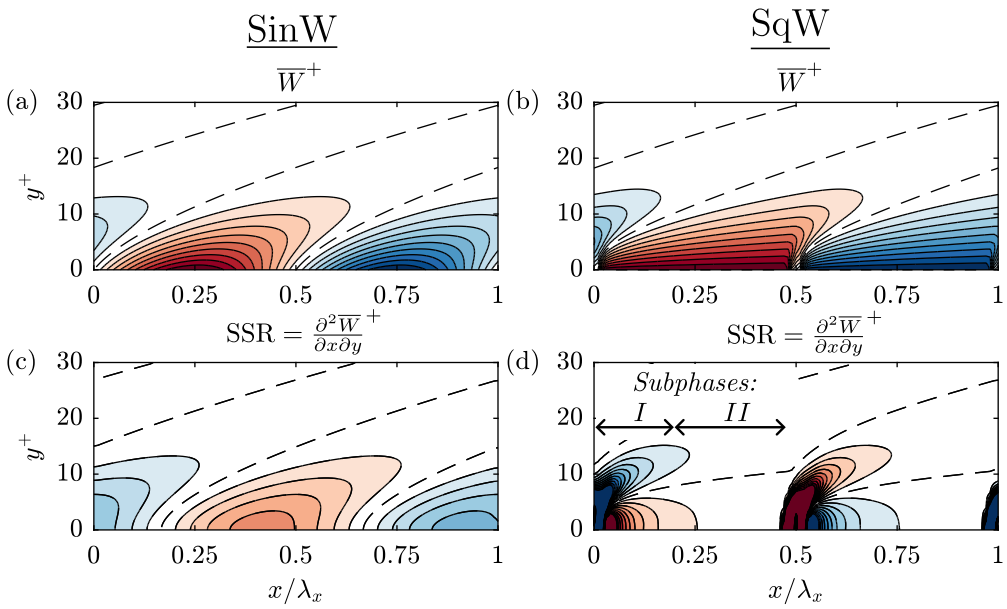

Figure 2: Phase-wise contours of the analytical solution for the (modified) Stokes layer (Knoop et al., 2024) at $\lambda_x^+ = 942$ for (a,c) SinW and (b,d) SqW forcing. (a,b) Spanwise velocity, contour level range: -1:0.1:1; (c,d) SSR, contour level range: -0.002:2 $\times 10^{-4}$:0.002. Adapted from Knoop et al. (2025).

($\partial\widetilde{W}/\partial y$), and is defined as $\partial^2\widetilde{W}/\partial\xi\partial y$. For spatial forcing, the phase corresponds to the streamwise coordinate, and SSR $= \partial^2\overline{W}/\partial x\partial y$. The tilde and overbar denote phase and time averaging, respectively. Regions of high SSR signify a rapid change in Stokes strain, which occurs twice during the forcing phase, and correspond to phase-wise locations where the wall velocity reverses direction (*i.e.*, W_w changes from positive to negative or vice versa). Regions of high-magnitude SSR have been previously correlated with a damping of the near-wall velocity streaks (Touber and Leschziner, 2012; Agostini et al., 2014). Agostini et al. (2015) proposed that the rapidly changing Stokes strain effectively breaks up the self-sustaining cycle (Jiménez and Pinelli, 1999) through a vortex stretching/titling mechanism. On the other hand, when the Stokes strain does not change for an extended phase, *i.e.*, SSR ~ 0, no interaction with the self-sustaining cycle occurs, and the turbulence was found to re-establish itself in the direction of the mean-strain vector $[\partial\widetilde{W}/\partial y,\ \partial(\overline{U}+\widetilde{U})/\partial y]$. This turbulence recovery can be linked to the recovery time scale of the near-wall streaks of $\mathcal{T}^+ \approx 50$ (Blesbois et al., 2013), which coincides with the optimum forcing period $T^+ \approx 100$ since high-magnitude SSR occurs twice per forcing phase. Analogous, for the spatial forcing ($\omega = 0$) concidered here, a convective lengthscale $\mathcal{L}^+ = \mathcal{T}^+ U_c^+ \approx 500$, matches with the optimum $\lambda_x^+ \approx 1000$ (Viotti et al., 2009).

Figure 2 differentiates the analytical solution of the spatial Stokes layer for SinW and SqW forcing. The SqW boundary condition is accounted for by using a modified Stokes-layer solution, which was previously validated using experiments in Knoop et al. (2024). In contrast to the gradual phase-wise variation of $\overline{W}$ for the SinW (Figure 2a), the wall velocity is piece-wise constant $\overline{W}$ over each half-phase for the SqW (Figure 2b), resulting in minimal streamwise variation in $\partial\overline{W}/\partial y$ (*i.e.*, SSR ~ 0). The difference between the two waveforms is clearly accentuated by the SSR behaviour in Figures 2(c,d). For the SqW a step change in the sign of W_w occurs at the half- and full-phase locations, *i.e.*, $x/\lambda_x = 0,\ 0.5,\ 1,\ \cdots$. Here, it produces high-magnitude impulses of SSR, while the constant wall-velocity segments yield SSR ~ 0, confirming negligible Stokes-strain variation.

Accordingly, two distinct SSR subphases can be distinguished for the SqW: *subphase-I*, characterised by high-magnitude SSR where the wall-forcing direction reverses, and *subphase-II*, marked by negligible SSR where W_w is constant. Owing to the waveform, the locations of forcing reversal remain fixed with λ_x, while the extent of constant $\pm W_w$ scales with λ_x, *i.e.*, the fetch and magnitude of subphase-I is wavelength-invariant while subphase-II extends in proportion to λ_x. Consequently, the asymmetry between the subphases increases when increasing the wavelength for the SqW forcing, which is illustrated when comparing the solution for $\lambda_x^+ = 942$ in Figure 2(d) with $\lambda_x^+ = 1884$ in Figure 5(c).

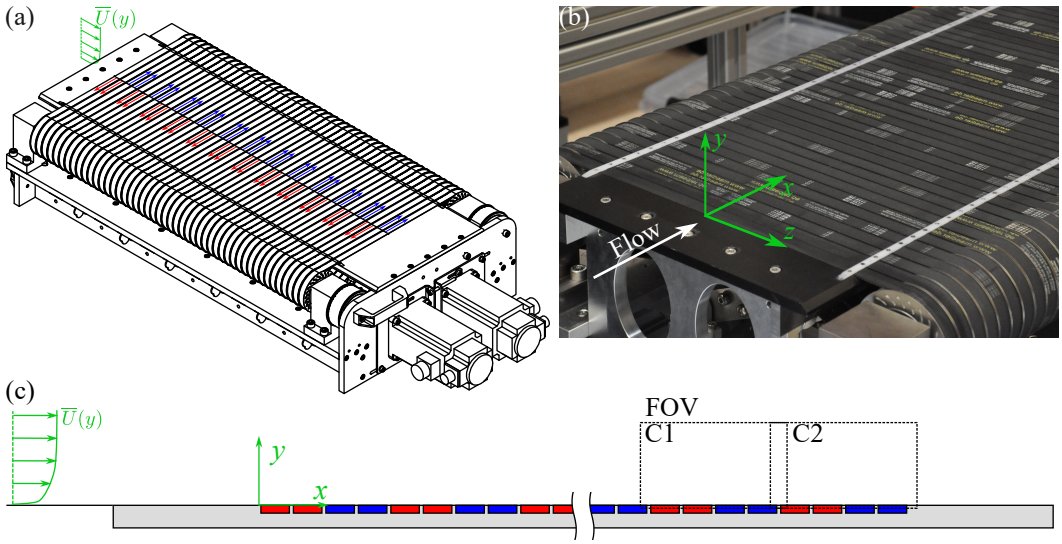

Figure 3: (a) Schematic of the experimental apparatus to impose a SqW-type boundary condition of spanwise wall velocity via spanwise-running belts. Red (blue) arrows/patches in (a,c) indicate a positive (negative) W_w. (b) A photograph that details the flush actuation surface with wall-embedded belts. (c) Schematic of the PIV experiment, showing the FOV where the forcing has fully established. (reproduced from Knoop et al., 2025).

In Knoop et al. (2025), we established a link between turbulence modification and the SSR characteristics of the SqW. We confirmed the hypotheses of Leschinger and co-workers; at the onset of actuation, an abrupt attenuation of Reynolds stresses could clearly be correlated with the impulsive imposition of SSR. Moreover, for the post-optimal case ($\lambda_x^+ = 1884$), where the fetch of subphase-II extended significantly beyond the recovery time/distance of the streaks ($\mathcal{L}^+ \gg 500$), the turbulence re-established itself. At a sufficient downstream distance on the actuator, where the forcing effect has fully established, the periodic attenuation-recovery cycle remained observable only for the post-optimal case, while the two (sub-)optimal cases showed a streamwise homogeneous response (see §3).

2 Experimental procedures

The experiments were previously reported in Knoop et al. (2025). In this section, the relevant aspects of the methodology are reiterated; the reader is referred to the original publication for further details. Experiments were conducted in an open-loop wind tunnel with a $0.6 \times 0.6\,\mathrm{m}^2$ cross-section. A ZPG TBL (see Dacome et al., 2024) develops over a 2.5 m fetch upstream of the actuation setup. The coordinate system used in this paper is located at the start of actuation (Figures 3b,c). Reynolds decomposition is applied as $U = \overline{U} + u$, and streamwise averaging over the forcing phase is denoted by $\langle \cdots \rangle_x$. The inflow TBL characteristics at $x = 0$ are: a boundary-layer thickness $\delta_0 = 69.9$ mm, a reference friction velocity $U_{\tau 0} = 0.207$ m/s, and a friction Reynolds number $Re_\tau \equiv U_{\tau 0}\delta_0/\nu = 960$.

The wall-forcing apparatus (refer to Figure 3a) comprises 48 spanwise-running belts, and extends $816 \times 294\,\mathrm{mm}^2$ or $\sim 11.7\delta_0 \times 4.2\delta_0$ in the streamwise and spanwise directions. The belts are 15 mm wide (in x) and have a 2 mm streamwise separation. Figure 3(b) shows how the belts are embedded in an aluminium surface plate to create a flush actuation surface. Strict tolerancing ensured that the gaps/steps on the actuation surface remain below 50 µm. Two 6 Nm servo motors (LCMT-18L02) provide direct-drive motion to the belts via a pulley system attached to two driving axes that rotate in the positive or negative spanwise directions. The pulleys can be engaged or disengaged, providing binary control over the spanwise wall velocity of each belt (*i.e.*, $\pm W_w$), which permits independent control of the forcing parameter λ_x and amplitude A^+, as previously illustrated in Figure 1.

An overview of the test cases and TBL characteristics is shown in Table 1. Four cases are studied: a non-actuated reference case, and three actuated cases at $\lambda_x^+ = 471$, 942, and 1884, all at matching $A^+ = 12$, by changing the number of belt elements S per full waveform, as 2, 4, and 8.

Flow statistics were measured using particle image velocimetry (PIV) in the streamwise-wall-normal plane. Knoop et al. (2025) also reports measurements at the onset of actuation; here, only the downstream

Inflow boundary layer characteristics				Actuation characteristics					
U_∞ (m/s)	$U_{\tau 0}$ (m/s)	δ_0 (mm)	Re_τ	S	λ_x (mm)	A (m/s)	λ_x^+	A^+	line style
5	0.207	69.9	960	–	–	–	–	–	
5	0.207	69.9	960	2	34	2.46	471	12.0	
5	0.207	69.9	960	4	68	2.46	942	12.0	
5	0.207	69.9	960	8	136	2.46	1884	12.0	

Table 1: Overview of the experimental conditions and actuation parameters; the first case refers to the non-actuated reference (reproduced from Knoop et al., 2025).

field-of-view (FOV) over the last eight belts (# 40 – 48) is considered, where the forcing effect has been fully established. As shown in Figure 3(c), two cameras were used to capture an FOV of $140 \times 49\,\mathrm{mm}^2$ ($x \times y$). 2000 uncorrelated snapshots of the TBL were acquired using sCMOS cameras ($2160 \times 2560\,\mathrm{px}^2$, 16 bit, pixel size 6.5 µm), which were mounted with 200-mm objectives at f/5.6. [U, V] velocity vectors were obtained using a cross-correlation in Gaussian interrogation windows of $16 \times 16\,\mathrm{px}^2$ at 75% overlap. The spatial resolution and vector pitch are 0.45 mm ($6.2\,\nu/U_{\tau 0}$) and 0.11 mm ($1.6\,\nu/U_{\tau 0}$), respectively.

Viscous scaling is applied using the kinematic viscosity ν, and either the reference (non-actuated) friction velocity $U_{\tau 0}$, denoted by a '+' superscript, or using the local (drag-reduced) friction velocity U_τ, denoted by a '*' superscript. Owing to the large-scale FOV, reliable data at $y^* < 5$ is absent, and therefore, U_τ was determined indirectly using a fit of the mean streamwise velocity to a composite profile. The composite profile of Chauhan et al. (2009) is modified to include an additional log-layer offset ΔB. The underlying assumption is that the change in U_τ due to the wall-forcing is captured by ΔB, while universality (*i.e.*, $u^* = y^*$) remains in the viscous sublayer, and is well accepted based on Gatti and Quadrio (2016). This indirect determination of U_τ was validated in Knoop et al. (2025, Appendix A) and has a 95% confidence interval of $U_\tau \pm 0.75\%$, which is comparable to the uncertainty for a composite fit of a canonical TBL (Rodríguez-López et al., 2015). Figures 4(a,b) shows the streamwise-averaged mean velocity profiles of FOV2, scaled using (a) the reference $U_{\tau 0}$, and (b) actual U_τ. The trends in $\langle \overline{U} \rangle_x$ are consistent with Gatti and Quadrio (2016), showing either (a) a reduction of $\langle \overline{U} \rangle_x^+$ in the near-wall region, or (b) an upward shift of the log layer for $\langle \overline{U} \rangle_x^*$. The corresponding drag reduction, $\mathrm{DR}\% = [1 - (U_\tau/U_{\tau 0})^2] \times 100$, is shown in tile Figure 4(c).

The theoretical input-power (P_{in}) required to drive the Stokes layer is calculated using the modified Stokes-layer solution (refer to §1.1; Knoop et al., 2024). By subtracting the input power from the power savings due to the DR effect, a theoretical measure for net-power saving (NPS) is obtained. The resulting NPS% is negative, in the order of −30% to −60%. This negative efficiency is attributed to the scaling of input power as $P_{in} \propto (A^+)^2$, whereas DR increases at a decreasing rate with A^+. An optimum (positive) NPS is, therefore, typically found at a lower forcing amplitude ($A^+ \approx 6$; Quadrio and Ricco, 2004; Quadrio et al., 2009). The present test cases are, however, not motivated by optimal performance; rather, the large forcing amplitude ($A^+ = 12$) was selected to yield a more pronounced turbulence modification, in view of the scope of our study being on the flow physics.

3 Phase-wise variation of turbulence for post-optimal forcing

The response of the TBL to sub-optimal (green; $\lambda_x^+ = 471$) and near-optimal (blue; $\lambda_x^+ = 942$) regimes is streamwise quasi-homogeneous (Knoop et al., 2025), which is reaffirmed here by the streamwise variation of C_f in Figure 5(a). In contrast, for the case of post-optimal conditions (red; $\lambda_x^+ = 1884$), a clear streamwise-periodic trend is observed.

This phase-wise variation is confirmed when assessing the turbulent stresses, in particular, the streamwise normal stress that signifies streaks and the near-wall dynamics. In Figure 5(b), the dispersive stress, $\overline{uu}^+(x,y) - \langle \overline{uu} \rangle_x^+(y)$, shows the deviation from its streamwise-averaged value, and reflects a periodic variation of attenuation (blue contours) and recovery (red contours). The (theoretical) SSR is shown in Figure 5(c), and confirms the conjectures regarding the turbulence modification (refer to §1.1). Downstream of the location where the wall velocity switches sign (the red/blue denote the belts and their $\pm W_w$), *i.e.*, subphase-I of high-magnitude SSR, the streamwise stress attenuates significantly, by over one viscous unit from its streamwise averaged value. On the other hand, at the end of subphase-II of SSR ~ 0, where W_w is constant, the turbulence re-establishes by a similar magnitude, owing to the $\mathcal{L}^+ \gg 500$ extension of this subphase in the post-optimal regime. This response is conjectured to be

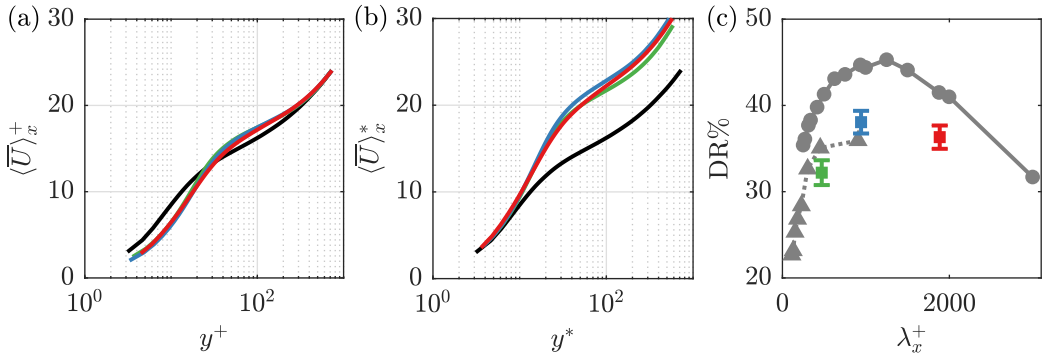

Figure 4: (a,b) Mean streamwise velocity profiles that are streamwise averaged across the phase; viscous scaling with (a) the non-actuated reference $U_{\tau 0}$ (b) the actual U_τ. (c) Variation of DR% with λ_x^+; coloured squares, present experiment (Table 1); circles, DNS at $Re_\tau = 200$ (Viotti et al., 2009); triangles, DNS at $Re_\tau = 906$ (Gatti and Quadrio, 2016), which is close to the present $Re_\tau = 960$. Reproduced from Knoop et al. (2025).

further accentuated as the wavelength increases to even larger values, and this remains a question for future research.

While this observed behaviour of the turbulent stresses agrees with the assumed SSR mechanics, the skin-friction coefficient shows an opposite, out-of-phase trend. During subphase-II, where the Reynolds stresses eventually recover, C_f continues to decline, while downstream of subphase-I, where the turbulence is strongly attenuated, a sharp increase in C_f occurs. We elucidate this behaviour in §4, by evaluating the development of an internal boundary layer (IBL) evident for the post-optimal case.

4 Stokes strain driven growth of an internal boundary layer

The IBL is identified using the indicator function, $\Xi \equiv \partial\overline{U}^+/\partial\ln(y^+)$, which corresponds to the wall-normal gradient of the $\overline{U}^+$ profile on a logarithmic scale. Numerous identification methods exist to determine the IBL thickness δ_i (see, *e.g.*, the comparison by Rouhi et al., 2019), however, these are tailored to step changes in roughness. These methods often identify changes in the logarithmic slope, which pertain far into the logarithmic layer, while the effects in this case are confined closer to the wall at $y^+ \lesssim 50$. Hence, a different identification method is used by evaluating the location of the peak of the indicator function:

$$\delta_i(x) \equiv \arg\max_y \frac{\partial\overline{U}(x,y)}{\partial\ln(y)}, \tag{2}$$

which represents the point of zero-curvature of the logarithmically-scaled $\overline{U}$ profile. Qualitatively, δ_i can be regarded as the transition between the viscous and buffer layer as the profile transitions from convex to concave. An increase in δ_i, thus, reflects a *thickening* of the viscous sublayer, an effect that is well established for the drag-reduced conditions imposed by transverse forcing (Jung et al., 1992; Ricco and Wu, 2004; Viotti et al., 2009).

Contours of the indicator function for the three forcing regimes are shown in Figures 6(b-d), while the identified δ_i^+ is marked by the white line, and Figure 6(a) repeats the skin-friction coefficients. In agreement with our previous observations, a significant phase-wise variation of the IBL structure is only reported for the post-optimal case (Figure 6d). Downstream of subphase-I, where W_w is constant, the IBL develops and grows from $\delta_i^+ \approx 10$ to 25. The growth of the IBL abruptly *colapses* when the spanwise wall velocity switches sign, and a new IBL develops downstream of this location. A clear correlation between δ_i and C_f is established, where the growth of the IBL represents a thickening of the viscous sublayer that is directly related to the decrease in C_f, and vice versa.

An approximate power-law scaling $\delta_i \propto \hat{x}^\alpha$ with exponent $\alpha \approx 0.45$ is found (black dashed lines in Figure 6d), where $\hat{x}$ is the local coordinate starting at the half-phase locations. The growth rate may not be directly compared to the literature, owing to the deviation in the definition of δ_i, but corresponds to typical values for roughness that has a wide spread $\alpha \sim 0.2 - 0.8$ that is sensitive to the identification method and individual datasets (Rouhi et al., 2019).

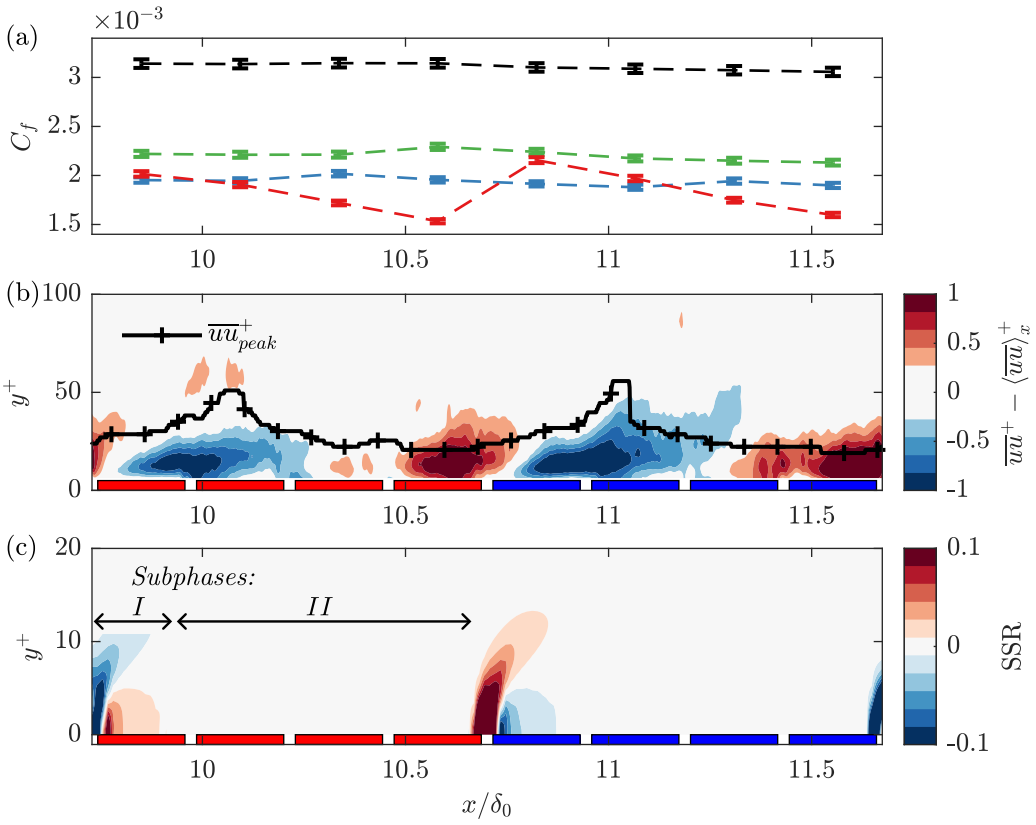

Figure 5: (a) Streamwise evolution of skin-friction coefficient (C_f) for the three forcing regimes, note only the markers correspond to its evaluation on the centre of each belt; dashed connecting lines are added for interpretability. For the post-optimal case $\lambda_x^+ = 1884$: (b) $\overline{uu} - \langle \overline{uu} \rangle_x^+$, *i.e.*, the deviation $\overline{uu}^+$ from its streamwise-averaged value, the black line y-location of the $\overline{uu}^+$ inner peak, and (c) analytical solution of SSR (Knoop et al., 2024). The shaded red (blue) patches in (b,c) denote belts and their positive (negative) spanwise wall velocity W_w. Adapted from Knoop et al. (2025).

The development of an IBL is typically observed for step changes in roughness (Rouhi et al., 2019; Li et al., 2021; Gul and Ganapathisubramani, 2022), and marks the non-equilibrium state of the TBL as it adjusts to the new boundary condition. In the case of spanwise forcing, the TBL reestablishes in the direction of mean strain (*i.e.*, $[\partial\overline{U}/\partial y,\ \partial\overline{W}/\partial y]$) when the Stokes strain is not changing for an extended fetch, *i.e.*, SSR ~ 0 (Touber and Leschziner, 2012). Consequently, the step-change in the sign of W_w corresponds to an impulsive reorientation of the TBL in the opposite transverse direction, driving the growth of a new IBL. Since a significant extent of near-zero SSR is required for the reorientation in the direction of mean strain, these dynamics only establish under post-optimal conditions.

5 Concluding remarks

We have confirmed the importance of the spanwise shear-layer, in particular the Stokes-strain rate (SSR), in the drag-reduction mechanism of transverse wall forcing. For the square wave (SqW) studied here, the SSR topology departs notably from the commonly studied sinusoidal forcing (SinW; 1). Localised regions of impulsive high-magnitude SSR occur at the location where the wall-forcing velocity (W_w) changes sign (subphase-I), whereas the rest of the half-phase is characterised by SSR ~ 0 (subphase-II).

A ZPG TBL at $Re_\tau = 960$ subjected to a streamwise-periodic SqW of spanwise wall velocity at $A^+ = 12$, displays a streamwise quasi-homogeneous response for the sub- and near-optimal cases at $\lambda_x^+ = 471$ and 942. The SSR variation only becomes apparent for the post-optimal case at $\lambda_x^+ = 1884$, which is marked by the periodic variation of a significant turbulence attenuation following subphase-I of high-magnitude SSR, and a recovery at the end of subphase-II, which agrees with the mechanisms proposed in the literature (Touber and Leschziner, 2012; Agostini et al., 2014, 2015). In the post-optimal

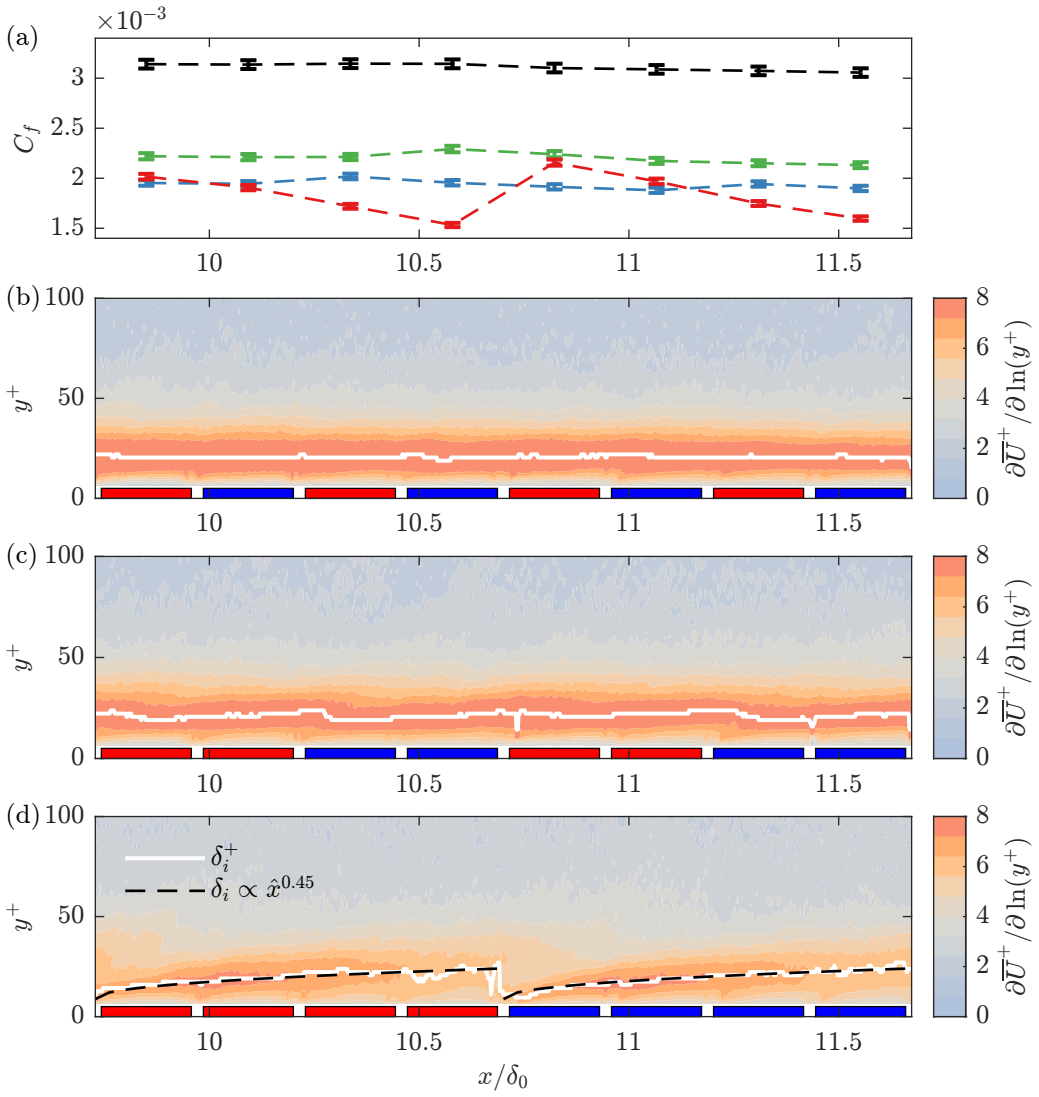

Figure 6: Streamwise evolution of (a) skin-friction coefficient (C_f). (b-d) shows the indicator function $\partial \overline{U}^+ / \partial \ln(y^+)$ and penetration height of the IBL $\delta_i^+(x)$, for (b) the sub-optimal regime $\lambda_x^+ = 471$, (c) the near-optimal regime $\lambda_x^+ = 942$, and (d) post-optimal regime $\lambda_x^+ = 1884$. The shaded red (blue) patches in (b-d) denote belts and their positive (negative) spanwise wall velocity W_w. The colourmap was derived from the sunset at the beach during the conference dinner. Adapted from Knoop et al. (2025).

regime, the skin-friction coefficient (C_f), at first sight, seems to be in contrast with the variation of the Reynolds stresses. C_f shows a sharp increase downstream of subphase-I, where the turbulence is attenuated, and subsequently, shows a continual decline over subphase-II, where the turbulence recovers.

The evolution of C_f is elucidated by the growth of an internal boundary layer (IBL) for $\lambda_x^+ = 1884$. The IBL develops right downstream of the location where the wall velocity changes sign, and grows from $\delta_i^+ \approx 10$ to 25 over the half-phase of constant W_w at a rate of $\delta_i \propto \hat{x}^{0.45}$. The increase in δ_i^+ is associated with a thickening of the viscous sublayer, and thereby, shows a clear correlation with the declining trend of C_f. The IBL then abruptly collapses upon the imposition of the next high-SSR event, and a new IBL is formed in the downstream region, accounting for the sharp increase in C_f after subphase-I. This periodic formation of IBLs indicates a non-equilibrium state, in which the TBL initially aligns with the direction of the mean strain – an alignment that emerges only for streamwise wavelengths $\lambda_x^+ \gg 1000$ (Touber and Leschziner, 2012) – and is then abruptly reversed at the step change in spanwise wall velocity.

Our results underscore the importance of properly distinguishing between the mean flow characteris-

tics (*i.e.*, C_f) and the turbulent stresses under non-equilibrium conditions. These quantities are often used interchangeably to assess the drag reduction potential of flow control strategies, yet they are observed to respond differently under these conditions. This initial characterisation of IBLs under drag-reduced conditions also highlights new research opportunities into the mechanisms that govern these non-equilibrium flows.

Acknowledgements
M.K. greatly appreciates the suggestion of Dr. Melika Gul to study the internal boundary layer development. Financial support was provided by The Netherlands Enterprise Agency under grant number TSH21002. R.D. gratefully acknowledges the financial support of the University of Melbourne's Postdoctoral Fellowship.

References

Agostini, L., Touber, E. and Leschziner, M. (2015), 'The turbulence vorticity as a window to the physics of friction-drag reduction by oscillatory wall motion', *Int. J. Heat Fluid Flow* **51**, 3–15.

Agostini, L., Touber, E. and Leschziner, M. A. (2014), 'Spanwise oscillatory wall motion in channel flow: drag-reduction mechanisms inferred from DNS-predicted phase-wise property variations at $Re_\tau = 1000$', *J. Fluid Mech.* **743**, 606–635.

Baron, A. and Quadrio, M. (1996), 'Turbulent drag reduction by spanwise wall oscillations', *Appl. Sci. Res.* **55**(4), 311–326.

Blesbois, O., Chernyshenko, S. I., Touber, E. and Leschziner, M. A. (2013), 'Pattern prediction by linear analysis of turbulent flow with drag reduction by wall oscillation', *J. Fluid Mech.* **724**, 607–641.

Chauhan, K. A., Monkewitz, P. A. and Nagib, H. M. (2009), 'Criteria for assessing experiments in zero pressure gradient boundary layers', *Fluid Dyn. Res.* **41**(2), 021404.

Choi, K. S. and Clayton, B. R. (2001), 'The mechanism of turbulent drag reduction with wall oscillation', *Int. J. Heat Fluid Flow* **22**(1), 1–9.

Dacome, G., Mörsch, R., Kotsonis, M. and Baars, W. J. (2024), 'Opposition flow control for reducing skin-friction drag of a turbulent boundary layer', *Phys. Rev. Fluids* **9**(6), 064602.

Gatti, D. and Quadrio, M. (2016), 'Reynolds-number dependence of turbulent skin-friction drag reduction induced by spanwise forcing', *J. Fluid Mech.* **802**, 553–582.

Gul, M. and Ganapathisubramani, B. (2022), 'Experimental observations on turbulent boundary layers subjected to a step change in surface roughness', *J. Fluid Mech.* **947**, A6.

Jiménez, J. and Pinelli, A. (1999), 'The autonomous cycle of near-wall turbulence', *J. Fluid Mech.* **389**, 335–359.

Jung, W. J., Mangiavacchi, N. and Akhavan, R. (1992), 'Suppression of turbulence in wall-bounded flows by high-frequency spanwise oscillations', *Phys. Fluids* **4**(8), 1605–1607.

Kempaiah, K. U., Scarano, F., Elsinga, G. E., Van Oudheusden, B. W. and Bermel, L. (2020), '3-dimensional particle image velocimetry based evaluation of turbulent skin-friction reduction by spanwise wall oscillation', *Phys. Fluids* **32**(8), 085111.

Kim, J. and Hussain, F. (1993), 'Propagation velocity of perturbations in turbulent channel flow', *Phys. Fluids A: Fluid Dyn.* **5**(3), 695–706.

Knoop, M. W., Deshpande, R., Schrijer, F. F. J. and van Oudheusden, B. W. (2025), 'Response of a turbulent boundary layer to steady, square-wave-type transverse wall-forcing', *Phys. Rev. Fluids* **10**(6), 064607.

Knoop, M. W., Hartog, F. H., Schrijer, F. F. J., van Campenhout, O. W. G., van Nesselrooij, M. and van Oudheusden, B. W. (2024), 'Experimental assessment of square-wave spatial spanwise forcing of a turbulent boundary layer', *Exp. Fluids* **65**(5), 65.

Li, M., De Silva, C. M., Chung, D., Pullin, D. I., Marusic, I. and Hutchins, N. (2021), 'Experimental study of a turbulent boundary layer with a rough-to-smooth change in surface conditions at high Reynolds numbers', *J. Fluid Mech.* **923**, A18.

Quadrio, M. and Ricco, P. (2004), 'Critical assessment of turbulent drag reduction through spanwise wall oscillations', *J. Fluid Mech.* **521**, 251–271.

Quadrio, M. and Ricco, P. (2011), 'The laminar generalized stokes layer and turbulent drag reduction', *J. Fluid Mech.* **667**, 135–157.

Quadrio, M., Ricco, P. and Viotti, C. (2009), 'Streamwise-travelling waves of spanwise wall velocity for turbulent drag reduction', *J. Fluid Mech.* **627**, 161–178.

Ricco, P. (2004), 'Modification of near-wall turbulence due to spanwise wall oscillations', *J. Turbul.* **5**(1), 024.

Ricco, P., Skote, M. and Leschziner, M. A. (2021), 'A review of turbulent skin-friction drag reduction by near-wall transverse forcing', *Prog. Aerosp. Sci.* **123**, 100713.

Ricco, P. and Wu, S. (2004), 'On the effects of lateral wall oscillations on a turbulent boundary layer', *Exp. Therm. Fluid Sci.* **29**(1), 41–52.

Rodríguez-López, E., Bruce, P. J. and Buxton, O. R. (2015), 'A robust post-processing method to determine skin friction in turbulent boundary layers from the velocity profile', *Exp. Fluids* **56**, 1–16.

Rouhi, A., Chung, D. and Hutchins, N. (2019), 'Direct numerical simulation of open-channel flow over smooth-to-rough and rough-to-smooth step changes', *J. Fluid Mech.* **866**, 450–486.

Touber, E. and Leschziner, M. A. (2012), 'Near-wall streak modification by spanwise oscillatory wall motion and drag-reduction mechanisms', *J. Fluid Mech.* **693**, 150–200.

Viotti, C., Quadrio, M. and Luchini, P. (2009), 'Streamwise oscillation of spanwise velocity at the wall of a channel for turbulent drag reduction', *Phys. Fluids* **21**, 115109.